Optical phonons as a testing ground for spin group symmetries

Felix Schilberth, M. Kondákor, D. Ukolov, A. Pawbake, K. Vasin, O. Ercem, Lilian Prodan, Vladimir Tsurkan, Alexander A. Tsirlin, C. Faugeras, P. Lemmens, K. Penc, Istvan Kézsmárki, Sándor Bordács, Joachim Deisenhofer

Angaben zur Veröffentlichung / Publication details:

Schilberth, Felix, M. Kondákor, D. Ukolov, A. Pawbake, K. Vasin, O. Ercem, Lilian Prodan, et al. 2026. "Optical phonons as a testing ground for spin group symmetries." *npj Quantum Materials* 11 (1): 26. https://doi.org/10.1038/s41535-026-00857-9.

npj | quantum materials

Article

Published in partnership with Nanjing University

https://doi.org/10.1038/s41535-026-00857-9

Optical phonons as a testing ground for spin group symmetries

F. Schilberth[1,2,11] ✉, M. Kondákor[3,4,11], D. Ukolov[5], A. Pawbake[6], K. Vasin[1,7], O. Ercem[1], L. Prodan[1], V. Tsurkan[1,8], A. A. Tsirlin[9], C. Faugeras[6], P. Lemmens[5], K. Penc[4], I. Kézsmárki[1], S. Bordács[1,2,10] & J. Deisenhofer[1] ✉

Lattice vibrations are highly sensitive to crystal symmetries and their changes across phase transitions. The latter can modify irreducible (co)representations and corresponding infrared and Raman selection rules of phonons. This concept is established for relativistic magnetic point groups, simultaneously transforming spatial and spin coordinates. However, in altermagnets described by non-relativistic spin groups with disjunct symmetry operations for both vector spaces, the phonon selection rules have remained unexplored. Here, we present a detailed study of the infrared- and Raman-active modes in the collinear antiferromagnet and altermagnet candidate $Co_2Mo_3O_8$. Comparing to ab initio calculations accurately capturing the eigenfrequencies, we identify all expected phonon modes at room temperature and deduce their selection rules using both symmetry approaches. Importantly, we observe the change of selection rules upon antiferromagnetic ordering, agreeing with the relativistic symmetry approach, while the spin group formalism predicts no changes. Therefore, optical phonons sensing the symmetry of the magnetic order can reveal if relevant magnon-phonon coupling is compatible with the spin-group approach or not.

The realm of compensated collinear antiferromagnets has been shaken by the introduction of the concept of altermagnetism[1] and many materials, which previously were regarded as benchmark "Néel" antiferromagnets such as the insulating rutiles MnF_2 and CoF_2 are now reconsidered for signatures of altermagnetism[2–5], in particular for non-relativistic spin splittings of electronic bands or splittings of magnons along general directions in the Brillouin zone. In this respect, MnTe appears to be among the most prominent realizations of such splittings[6–9], while the altermagnetism in RuO_2 remains controversial[10–12].

In terms of symmetry, altermagnets and the breaking of Kramers degeneracy at a general point in the Brillouin zone are described by using the spin group concept introduced in the 1960s and classified by Litvin and Opechowski[13–16], which separates spatial symmetry operations and symmetry elements in spin space corresponding to the non-relativistic limit with zero spin-orbit coupling.

This limit is in clear contrast to the concept of the Shubnikov magnetic space and point groups. Those are commonly used to determine the transformation properties of observables by applying the Neumann principle and selection rules for excitations. The magnetic point group elements simultaneously leave the structural and the spin configuration invariant, i.e., a relativistic setting with non-zero spin-orbit coupling is imposed[17].

We want to compare these two symmetry approaches by investigating experimentally and theoretically the optical phonons and their selection rules in $Co_2Mo_3O_8$, which belongs to the family of polar molybdenum oxides $A_2Mo_3O_8$ (A = Mn, Fe, Co, Ni, Zn). These polar materials exhibit different magnetically ordered ground states, which can be tuned by external magnetic fields or doping[18–28]. For $Fe_2Mo_3O_8$, low-lying chiral phonons and magnon-polariton excitations in the THz frequency range have been reported[29–32], which exhibit non-reciprocal directional dichroism[25,32]. Only recently, it was recognized that the collinear antiferromagnetic (AFM)

[1]Experimental Physics V, Center for Electronic Correlations and Magnetism, Institute for Physics, University of Augsburg, Augsburg, Germany. [2]Department of Physics, Institute of Physics, Budapest University of Technology and Economics, Müegyetem rkp. 3., H-1111 Budapest, Hungary. [3]Department of Theoretical Physics, Institute of Physics, Budapest University of Technology and Economics, Budapest, Hungary. [4]Institute for Solid State Physics and Optics, HUN-REN Wigner Research Centre for Physics, Budapest, Hungary. [5]Institute of Condensed Matter Physics, TU Braunschweig, Braunschweig, Germany. [6]LNCMI, UPR 3228, CNRS, EMFL, Université Grenoble Alpes, Grenoble, France. [7]Institute for Physics, Kazan (Volga region) Federal University, Kazan, Russia. [8]Institute of Applied Physics, Moldova State University, Chisinau, Republic of Moldova. [9]Felix Bloch Institute for Solid-State Physics, Leipzig University, Leipzig, Germany. [10]HUN-REN-BME Condensed Matter Physics Research Group, Budapest University of Technology and Economics, Müegyetem rkp. 3., H-1111 Budapest, Hungary. [11]These authors contributed equally: F. Schilberth, M. Kondákor. ✉e-mail: felix.schilberth@physik.uni-augsburg.de; joachim.deisenhofer@physik.uni-augsburg.de

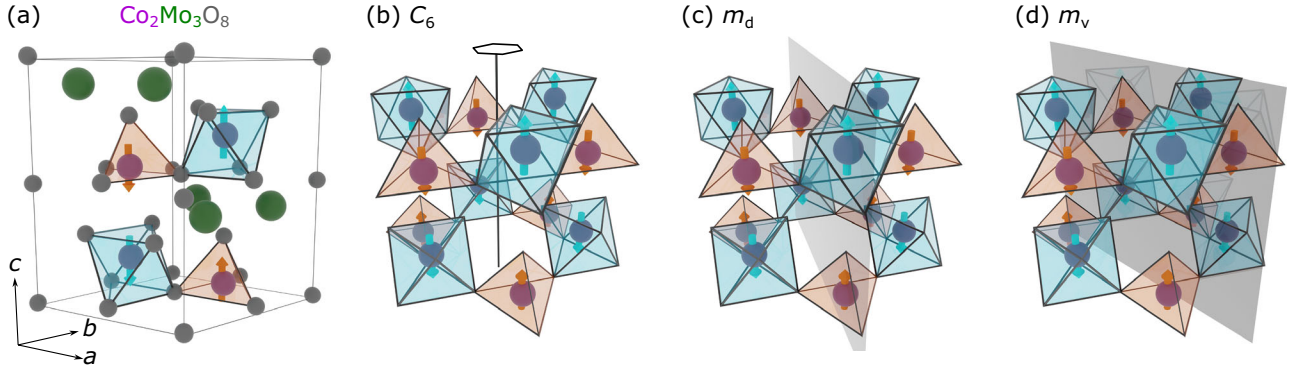

Fig. 1 | Crystal structure and magnetic ordering of $Co_2Mo_3O_8$. a Crystallographic and magnetic unit cell with two formula units illustrating the collinear $q = 0$ antiferromagnetic spin order. Symmetry elements generating the crystallographic point group $6mm$: **b** the sixfold rotation axis C_6, **c** the diagonal mirror plane $m_d = \{m_{100}, m_{010}, m_{1\bar{1}0}\}$, and **d** the vertical mirror plane $m_v = \{m_{110}, m_{120}, m_{2\bar{1}0}\}$. When combined with a half-translation along the c axis, the C_6 forms a screw axis, and the m_v becomes a glide plane. They are symmetry elements of the space group $P6_3mc$ (No.186).

phases of $Co_2Mo_3O_8$ and $Fe_2Mo_3O_8$ fulfill the necessary criteria for altermagnets[33,34].

In the paramagnetic regime, $Co_2Mo_3O_8$ and the other family members $A_2Mo_3O_8$ (A = Mn, Fe, Co, Ni, Zn) crystallize in the non-symmorphic polar hexagonal space group $P6_3mc$ (#186), featuring a built-in polarization along the c-axis. The unit cell is shown in Fig. 1a. The A^{2+} ions are responsible for magnetism, with half of them occupying the corner-sharing tetrahedral (A) and the other half the octahedral (B) sites. The Mo ions build non-magnetic trimers[19,35,36]. Upon cooling, $Co_2Mo_3O_8$ undergoes collinear AFM order at $T_N = 39$ K[21,24–26,28] with all spins aligned parallel to the c-axis as illustrated in Fig. 1, as does the sister compound $Fe_2Mo_3O_8$ at $T_N = 60$ K[18,19]. No structural symmetry changes were observed upon entering the AFM phase for both compounds[21,37], making them ideal candidates to study symmetry changes due to the collinear AFM ordering.

First, we analyze the symmetry properties and selection rules in $Co_2Mo_3O_8$ for Raman- and infrared (IR)-active phonons in terms of the relativistic magnetic point group and the non-relativistic spin group approach. Then, we discuss the optical modes observed by IR- and Raman spectroscopy and identify the phonons by comparison of the eigenfrequencies with ab initio calculations and conclude on the applicability of the two symmetry concepts for $Co_2Mo_3O_8$.

Results

Symmetries of the paramagnetic and the collinear magnetic state of $Co_2Mo_3O_8$

The crystallographic point group in both the paramagnetic and magnetically ordered phases is $G = 6mm$ (C_{6v}), which contains twelve symmetry operations grouped into six conjugacy classes:

$$\begin{aligned}\mathbf{G} &= \{E\} + \{C_6^+, C_6^-\} + \{C_3^+, C_3^-\} + \{C_2\} \\ &\quad + \{m_{100}, m_{010}, m_{1\bar{1}0}\} + \{m_{110}, m_{120}, m_{2\bar{1}0}\} \\ &= \{E\} + \{C_6\} + \{C_3\} + \{C_2\} + \{m_d\} + \{m_v\}.\end{aligned} \quad (1)$$

Figure 1b–d shows the generators of the $6mm$ point group. Note that the C_6 sixfold and the C_2 twofold rotations, as well as the m_v mirror planes are non-symmorphic: each must be accompanied by a half-translation ($c/2$) along the z-axis, transforming them into screw-axis rotations and glide-plane reflections in the non-symmorphic space group $P6_3mc$.

Superimposing the collinear spin configuration of the magnetically ordered state onto the corresponding A- and B-sites occupied by the magnetic ions, one can follow two routes. (i) The relativistic route, where finite spin-orbit interactions lead to a description using magnetic space and point groups. For $Co_2Mo_3O_8$, this is determined by the unitary halving subgroup $\mathbf{H} = 3m$ of $\mathbf{G}$, yielding the magnetic point group $\mathbf{M} = 6'm'm$. Due to the Lorentz-invariant relativistic framework, the simultaneous transformation of spatial coordinates and spin degrees of freedom naturally arises from the spin-orbit coupling. Alternatively, we can take the non-relativistic route (ii), where we neglect spin-orbit effects and describe the order in terms of spin groups, as is done for altermagnets. If we infer the collinear spin arrangement on the two sublattices which in Litvin's notation is denoted by a superscript $\bar{1}$ for crystallographic symmetries connecting the two sublattices[16], we obtain the spin group $\mathbf{G}_s = {}^{\bar{1}}6^{1}m^{\bar{1}}m$ (The classification for both approaches is detailed in Supplement I A).

Remarkably, the group-theoretical condition for altermagnetism can be expressed using irreducible representations of the crystallographic point group $\mathbf{G}$ and the primary antiferromagnetic order parameter given by a component of the Néel vector $\mathbf{L}$: If this component of $\mathbf{L}$ belongs to a one-dimensional real representation of $\mathbf{G}$, which remains invariant under all operations preserving the momentum $\mathbf{k}$, then the antiferromagnetic order is compatible with altermagnetism[38,39]. In $Co_2Mo_3O_8$, the magnetic ordering exhibits a complex structure due to the presence of spins located on both tetrahedral (A sites) and octahedral (B sites) sublattices, with Néel order established independently on each sublattice. The Néel vector can be defined as $\mathbf{L} = \mathbf{L}_A + \mathbf{L}_B = \frac{1}{2}(\mathbf{M}_1 - \mathbf{M}_2)$, where $\mathbf{L}_X = \frac{1}{2}(\mathbf{M}_{1X} - \mathbf{M}_{2X})$ denotes the Néel vectors on $X = A, B$ sites, and subscripts 1 and 2 denote the magnetization of the magnetic sublatices (specifically, subscript 1 corresponds to the up-spin magnetizations and 2 to the down-spin magnetizations)[27]. Depending on the choice of the isomorphism between $\mathbf{G}$ and the abstract group $6mm$, the Néel vector transforms according to either the irreducible representation B_1 or B_2 of $6mm$ (see Table SI in Supplement I A). In both scenarios, $\mathbf{L}$ changes sign only under symmetry operations that do not map $\mathbf{k}$ to $-\mathbf{k}$. This implies that time reversal does not remain a symmetry even in combination with a partial translation or inversion, hence $Co_2Mo_3O_8$ meets the group-theoretical requirement for altermagnetism. The inversion symmetry—the other key symmetry connecting states with opposite momentum—is already broken by the crystal structure of $Co_2Mo_3O_8$ in the paramagnetic state. The key difference between the classifications (i) and (ii) for our study is how the magnetic groups modify the corepresentations and selection rules for optically active phonons, which we detail in the following.

Irreducible (co)representations and selection rules for IR- and Raman-active phonons

In this section, we discuss phonon selection rules in $Co_2Mo_3O_8$ by considering the symmetry of the paramagnetic and magnetically ordered phases. In particular, we will outline the difference in phonon selection rules deduced from the non-relativistic spin point group in comparison with the magnetic point group. While unitary representation theory adequately describes crystallographic point groups, magnetic point groups require corepresentation theory to include the antiunitary operations. Corepresentations play an analogous role for magnetic groups to that of unitary

representations for non-magnetic groups and are conventionally denoted as $D\Gamma$[17]. The symmetry requirements for IR- and Raman-active modes are summarized in Supplement I B.

Explicitly, the number and symmetry of the allowed optical phonon modes for paramagnetic $Co_2Mo_3O_8$ with two formula units in the primitive unit cell[21] are given by

$$\begin{aligned}\Gamma = {} & 9A_1(z;xx,yy,zz) + 12E_1(x,y;xz,yz) && \text{(IR + Raman)}\\ & +13E_2(x^2-y^2,xy) && \text{(Raman)}\\ & +A_1 + E_1 && \text{(acoustic)}\\ & +3A_2 + 10B_1 + 3B_2 && \text{(silent)},\end{aligned} \tag{2}$$

where the IR active modes correspond to the linear coordinate functions of a polar vector and the Raman active modes to the quadratic coordinate functions of the polar second-rank Raman tensor. Hence, in the IR experiments, nine A_1-modes should be observable for $\mathbf{E}^{\omega}\|c$ and in the Raman channel these modes should appear exclusively in the configurations $x(zz)\bar{x}$ or $y(zz)\bar{y}$. The 12 E_1-modes are IR-active for $\mathbf{E}^{\omega}\|a$ and can be identified in the Raman configurations $y(xz)\bar{y}$ or $x(yz)\bar{x}$. The 13 E_2 modes are only Raman active and can be singled out in the Raman channel $z(xy)\bar{z}$. Thus, the standard experimental procedure to identify the IR and Raman-active phonon modes is to measure IR reflectivity in the two polarization configurations and Raman scattering in the three different Raman configurations, as it has been performed in previous IR and Raman studies of the isostructural compound $Fe_2Mo_3O_8$[37,40]. In addition, we perform Raman measurements in the $z(xx)\bar{z}$ configuration, which, in the paramagnetic phase, allows the observation of the A_1 and E_2 modes.

Upon magnetic ordering, the symmetry is lowered from the paramagnetic symmetry group to the magnetic space group $P6'_3m'c$ with the magnetic point group $6'm'm$, but the primitive unit cell and, consequently, the total number of normal modes remain unchanged. In analogy to the paramagnetic case, the selection rules have to be determined now using the irreducible corepresentations of the antiferromagnetic state given by

$$\begin{aligned}D\Gamma = {} & 19DA_1(z;xx,yy,zz) && \text{(IR + Raman)}\\ & +25DE(x,y;xx,yy,xy,xz,yz) && \text{(IR + Raman)}\\ & +DA_1 + DE && \text{(acoustic)}\\ & +6DA_2 && \text{(silent)}.\end{aligned} \tag{3}$$

The corresponding symmetry adapted Raman tensors for the 58 black-and white magnetic point groups are given by Cracknell[41] and summarized for $Co_2Mo_3O_8$ in Table SV in Supplement I A. The A_1 and B_1 modes will be contained in the corepresentation DA_1, the A_2 and B_2 modes form the class DA_2, and E_1 and E_2 will form the DE class. Consequently, upon cooling into the AFM phase, one may expect many more modes to become visible both in IR- and Raman measurements.

As outlined above, $Co_2Mo_3O_8$ is a candidate for altermagnetism. Therefore, we may ask whether we can obtain different selection rules if we consider spin-group symmetries instead of the usual magnetic point groups, and if they are realized in the material. As shown in Ref. 42, the spin point group ${}^{\bar{1}}6^{\bar{1}}m^1m$ introduces new irreducible corepresentations compared to the magnetic point group (both tabulated in Table SIII in Supplement I A), possibly giving rise to new or additional selection rules. To derive these for IR and Raman active phonons, we begin by comparing the character tables of the crystallographic point group $6mm$ (Table SI), its magnetic counterpart $6'm'm$ (Table SII), and full spin group ${}^{\bar{1}}6^{\bar{1}}m^1m$ (Table SIII). Introducing magnetic order halves the number of unitary operations and promotes the remaining irreps of $6mm$ into co-irreps of the unitary subgroup $3m$. Antiunitary elements follow the co-representation relation

$$D\Gamma(au) = D\Gamma(a)(D\Gamma(u))^{\star}, \tag{4}$$

instead of the usual product rule $\Gamma(uv) = \Gamma(u)\Gamma(v)$ with u, v denoting unitary and a antiunitary symmetry elements[17]. However, as soon as spin and real space components decouple and new unitary transformations arise, one can associate each unitary operation of the spin group $[s||g]$ in ${}^{\bar{1}}6^{\bar{1}}m^1m$ with g in $6mm$. Here, s is the spin space operation and g the real space operation of the spin group symmetry. As a result, all irreps of $6mm$ can be extended to co-irreps in ${}^{\bar{1}}6^{\bar{1}}m^1m$ – these are given by $D\Gamma_1 - D\Gamma_6$ in Table SIII.

Because the electric dipole polarization $\mathbf{p}$, the electric field of light $\mathbf{E}^{\omega}$, and the symmetric Raman tensor $\widehat{R}$ transform purely under spatial operations as shown in Supplement I C, they correspond exclusively to the six co-irreps $D\Gamma_1 - D\Gamma_6$ that can be directly associated to the irreducible representations of the crystallographic point group (or the co-irreps of the paramagnetic group). Consequently, the spin group analysis reproduces exactly the crystallographic selection rules of $6mm$ seen in the paramagnetic phase.

At the microscopic level, phonons sense magnetic order via spin-phonon interactions arising from slight distortions of the ligand environment around each magnetic ion. These terms enter the unperturbed Hamiltonian and, if they respect the full spin group symmetry, will enforce the corresponding spin group selection rules with respect to the electric dipole perturbation $\mathbf{E}\cdot\mathbf{p}$. Conversely, if the spin-phonon coupling requires the coupled spin and real-space transformations, then the allowed IR and Raman transitions revert to those prescribed by the magnetic point group symmetry alone.

In conclusion, our analysis demonstrates that the selection rules of the corresponding spin group for IR and Raman active phonons are identical to those determined by its crystallographic point group. As a result, such spectroscopic probes can reveal the significance of spin-orbit coupling through magnon-phonon interactions and indicate whether relativistic effects can be neglected for phonon and magnon excitations. As diffraction experiments $Co_2Mo_3O_8$ found that the crystallographic point group remains unchanged upon magnetic ordering[21], the non-relativistic description would suggest that there are no qualitative changes between the paramagnetic and antiferromagnetic phases. Actually, this scenario seems to apply to many altermagnetic candidates[43]. For $Co_2Mo_3O_8$, however, this result clearly contrasts with the predictions from the magnetic point-group analysis presented in Eq. (3), where we expect the relativistic effects to show up in the spectral properties.

Raman and infrared active modes in $Co_2Mo_3O_8$

In this section, we will compare the measured IR- and Raman spectra of $Co_2Mo_3O_8$ obtained in the paramagnetic phase (at 295 K or 300 K) and in the antiferromagnetic phase (at 5 K or 10 K) with the calculated eigenfrequencies obtained by ab initio calculations, in order to identify newly activated modes of the magnetically ordered state. As the overall number of expected phonon modes remains constant across the magnetic transition, we will refer to the phonon modes using the nomenclature of the irreducible representations of the non-magnetic crystallographic point group for clarity reasons. However, one should always be aware that modes which belong to different irreducible representations in the paramagnetic state may belong to the same irreducible corepresentation in the magnetically ordered state, as discussed above.

It is also important to note that we compare the Raman scattering results with the expected selection rules as given by Eqs. (2) and (3) derived for the approximate first-order non-resonant Raman cross section for non-polar modes[44,45]. Strictly speaking, these Raman selection rules are only justified for the non-polar E_2-modes in the paramagnetic phase, but the main reported effects of the internal electric field originating from polar phonons in uniaxial crystals like $Co_2Mo_3O_8$ is the lifting of degeneracies and shifts of such modes for scattering angles away from the backscattering configuration used in this study[44,46,47]. Hence, we do not expect to observe a modification of the selection rules due to the polar nature of the phonons.

Given the large number of expected modes, we start with the nine phonons of A_1 symmetry, which should be active in the IR experiment for light polarization $\mathbf{E}^{\omega}\|c$ and in the Raman scattering configuration $y(zz)\bar{y}$,

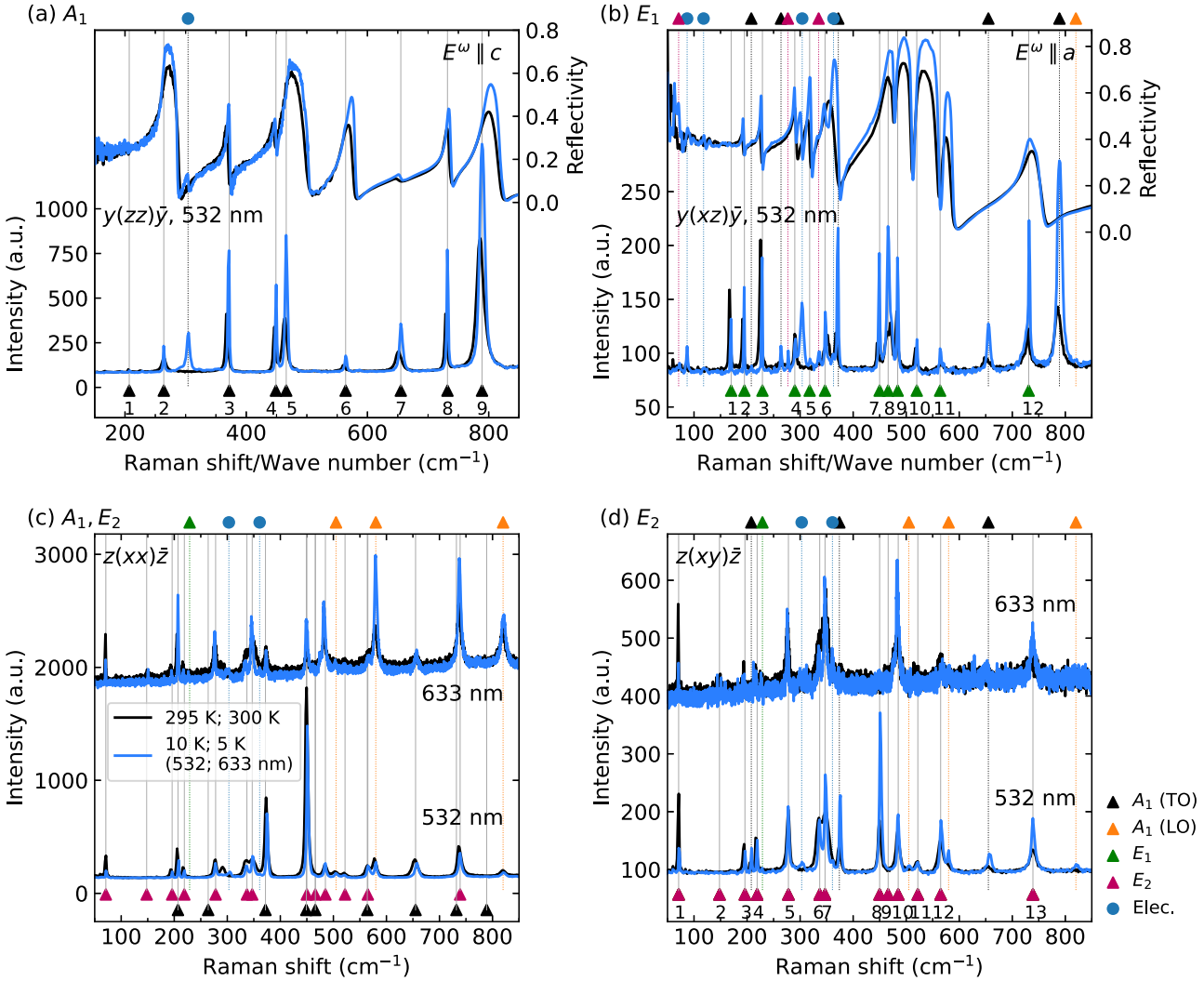

Fig. 2 | Optical phonon spectra in $Co_2Mo_3O_8$. Comparison of Raman and far-infrared reflectivity spectra at 295 K/300 K (black) and 10 K/5 K (blue) in **a** scattering configuration $y(zz)\bar{y}$ (532 nm) and light polarization $\mathbf{E}^\omega \| c$ corresponding to the irreducible A_1 representations, **b** in scattering configuration $y(xz)\bar{y}$ (532 nm) and light polarization $\mathbf{E}^\omega \| a$ corresponding to the irreducible E_1 representation. **c**, **d** Comparison of Raman spectra at laser wavelengths of 532 nm and 633 nm in scattering configurations $z(xx)\bar{z}$ allowing for the observation of E_2 and A_1 modes, and $z(xy)\bar{z}$ corresponding to the irreducible E_2 representations of the paramagnetic phase, respectively. The determined eigenfrequencies of phonon modes expected for each configuration in the paramagnetic phase are indicated by upward triangles at the bottom of the individual panels. Symbols at the top of the panels indicate modes different from expected modes of the paramagnetic phase as described in the text.

where no other vibrational Raman modes should be active. The corresponding reflectivity and Raman spectra are shown in Fig. 2a. At room temperature, we identify eight clearly visible resonances in the IR reflectivity and nine modes in the Raman spectrum, where the lowest-lying mode is very weak in the Raman spectrum and not observable in reflectivity. The number of modes is in good agreement with the expected A_1 phonons, and they remain visible upon cooling into the magnetically ordered phase. When entering into the magnetic phase, one additional mode emerges at 304 cm^{-1}. The eigenfrequencies of all excitations were determined from the peak maxima for the Raman modes and from a fit with Lorentzian lineshapes for the reflectivity spectra (see Supplement III) and are listed in Table 1 together with the calculated eigenfrequencies for the A_1 phonons at low temperatures (the complete list of calculated eigenfrequencies is given in Table SVI in Supplement II). For the IR active A_1 modes, we list both the transverse optical (TO) eigenfrequencies and the longitudinal optical (LO) eigenfrequencies as determined from the reflectivity fit (see Supplement III). The TO modes are to be compared with the calculated values, while the LO frequencies will be important for Raman mode assignment in other configurations discussed below. Based on the good agreement of calculated and observed eigenfrequencies of the nine excitations observed at 295 K and 10 K, we identify these modes with the A_1 phonons and conclude that we observe no deviations from the approximate phonon selection rules in Eqs. (2) and (3). The additional mode at 304 cm^{-1} might be one of the B_1 phonons, which are predicted to fall into the same corepresentation class as the A_1 modes. However, we discard this possibility, as none of the calculated eigenfrequencies of the B_1 phonons is in agreement with the observed mode, and we found that this mode undergoes significant changes in an applied magnetic field. Therefore, we assign it to be of electronic origin stemming from Co^{2+}-multiplet excitations, similar to modes reported for the isostructural material $Fe_2Mo_3O_8$ in its magnetically ordered phase[32,37,40].

We will follow the same line of reasoning in the assignment of the modes in the other measurement configurations. The richest spectra are observed for infrared reflectivity measured with light polarization $\mathbf{E}^\omega \| a$ and in the Raman scattering configuration $y(xz)\bar{y}$, which are shown together in Fig. 2b. The eigenfrequencies of all observed modes are listed in Table 2 and we can identify four classes of excitations.

The first class contains the modes visible at 295 K and at 10 K, which are in good agreement with the expected frequencies of the twelve E_1(i) phonons $i = 1, \ldots, 12$. Note that modes $E_1(1)$ and $E_1(7)$ are only observed in Raman scattering. The second class contains three modes, which only

Table 1 | IR and Raman excitations for $E^{\omega}||c$ and $y(zz)\bar{y}$

IR (TO)		Raman		Mode assignment	IR (LO)	
$E^{\omega}||c$		$y(zz)\bar{y}$		$A_1(i)$	$E^{\omega}||c$	
295 K	10 K	295 K	10 K	i = 1, …, 9 (calc.)	295 K	10 K
–	–	*205*	*207*	204	–	–
264	*263*	*264*	*264*	271	290	287
367	*370*	*369*	*372*	356	371	374
446	*448*	*446*	*449*	453	447	449
467	*468*	*463*	*466*	456	500	504
565	*569*	*560*	*564*	564	578	582
653	*656*	*652*	*655*	652	655	657
731	*733*	*729*	*732*	723	737	739
793	*793*	*786*	*789*	811	819	822
–	304	–	304	electronic	–	304

Comparison of experimental IR (TO and LO) and Raman active excitation frequencies (in cm^{-1}) in $Co_2Mo_3O_8$ measured for light polarization $\mathbf{E}^{\omega}||c$ and in the Raman configuration $y(zz)\bar{y}$, respectively. The experimental eigenfrequencies measured at 295 K and 10 K are compared with theoretical ab initio values for the nine A_1 modes. Numbers in italic fonts indicate the allowed observed modes.

Table 2 | IR and Raman excitations for $E^{\omega}||a$ and $y(xz)\bar{y}$

IR (TO)		Raman		Mode assignment
$E^{\omega}||a$		$y(xz)\bar{y}$		
295 K	10 K	295 K	10 K	$E_1(i)$ i = 1, …, 12 (calc.)
–	–	*167*	*170*	166
191	*193*	*191*	*195*	186
225	*227*	*225*	*229*	224
289	*290*	*290*	*291*	277
315	*317*	*314*	*318*	313
354	*345*	*352*	*347*	355
–	–	*445*	*450*	463
465	*463*	*470*	*466*	467
487	*486*	*482*	*484*	480
527	*521*	*517*	*520*	528
568	*570*	*561*	*564*	575
737	*728*	*730*	*731*	760
–	*72**	–	*72*	E_2(1) at 71 (exp.)
–	–	–	*277*	E_2(5) at 278 (exp.)
–	–	–	*335*	E_2(6) at 337 (exp.)
–	–	205	208	A_1(1) at 207 (TO)
–	–	264	264	A_1(2) at 264 (TO)
–	–	367	372	A_1(3) at 372 (TO)
–	–	650	655	A_1(7) at 655 (TO)
–	–	786	789	A_1(9) at 789 (TO)
–	–	–	820	A_1(9) at 822 (LO)
–	41*	–	–	electronic
–	87	–	87	electronic
–	118	–	118	electronic
–	301	–	304	electronic
–	361	–	363	electronic

Comparison of experimental IR (TO) and Raman active excitation frequencies (in cm^{-1}) in $Co_2Mo_3O_8$ measured for light polarization $\mathbf{E}^{\omega}||a$ and in the Raman configuration $y(xz)\bar{y}$, respectively. The IR eigenfrequencies marked with * were observed by THz-transmission spectroscopy. Mode assignment is made by comparison with calculated phonon eigenfrequencies for E_1 modes and by comparing to experimental values from other Raman measurement configurations. Numbers in italic fonts indicate the allowed observed modes.

emerge upon cooling below the Néel temperature and appear mostly in the Raman channel. Three of these modes can be identified as E_2 phonon modes, which are expected to be observable in both the $y(xz)\bar{y}$ and the $z(xy)\bar{z}$ channels in the magnetically ordered phase as a part of the *DE* copresentation. In addition, mode $E_1(2)$ at 72 cm^{-1} was observed independently in the IR channel by THz-transmission spectroscopy (see Fig. S3). This confirms the expected changes of selection rules due to symmetry breaking by magnetic ordering as derived from the analysis of the relativistic magnetic point group $6'm'm$. The third class of modes contains six modes, which are observed by Raman scattering only. Five of them are visible both at 295 K and at 10 K with eigenfrequencies coinciding with the observed TO eigenfrequencies of the identified A_1 phonons (compare Fig. 2a and Table 1), while the highest lying one at 820 cm^{-1} is only visible below T_N but agrees nicely with the LO eigenfrequency of mode $A_1(9)$. A_1 phonons are not allowed in this configuration according to the selection, but their strength and linewidth are comparable to that of the allowed modes in this configuration. As the appearance is restricted to the Raman spectra only, but they are observed already at 295 K, we attribute their Raman activity and the breaking of the selection rules given in Eqs. (2) and (3) to resonant Raman effects, which can occur if the laser frequency is resonant with an electronic excitation frequency of the material. Resonant Raman scattering processes can be very complex, but are known to enhance intensities and lead to a breaking of selection rules, including the appearance of LO modes[48,49]. The observation of such effects is interesting by itself, but not the main objective of this paper. Hence, we discuss our assignment to resonant Raman effects and why we discard impurity-induced symmetry breaking for the forbidden A_1 modes in detail in Supplement IV.

The fourth class of modes is assigned to electronic modes, which become both IR and Raman active in the magnetically ordered phase. Besides the mode at 304 cm^{-1}, which was already observed for $\mathbf{E}^{\omega}||c$ and $y(zz)\bar{y}$ at low temperatures, there are two modes at 87 cm^{-1} and 118 cm^{-1}, which have previously been shown to split in an applied magnetic field reported in THz transmission measurements[25]. Similar to the mode at 304 cm^{-1}, the new mode at 363 cm^{-1} was found to exhibit significant changes in an applied magnetic field, which cannot be reconciled with phononic behavior and supports our assignment.

To complete the analysis of Raman selection rules, we show the spectra for the Raman scattering configurations $z(xx)\bar{z}$ and $z(yx)\bar{z}$ in Fig. 2c, d, respectively, for a laser wavelength of 532 nm (as in panels (a) and (b)) together with the spectra taken at a wavelength of 632.8 nm. Raman spectra taken in these configurations at 514.3 nm and 473 nm are shown in Fig. S5 in Supplement III. All observed eigenfrequencies for both configurations and all wavelengths are summarized in Table 3. Following the selection rules, the spectra in $z(yx)\bar{z}$ configuration should identify the 13E_2 phonons at room temperature, while for $z(xx)\bar{z}$ both E_2 and A_1 phonons are allowed at room temperature already. At low temperature, all modes of corepresentations DA_1 (corresponding to all A_1 and B_1 modes) and *DE* (corresponding to all E_1 and E_2) are allowed in $z(xx)\bar{z}$, while in $z(yx)\bar{z}$ the observed excitations should be restricted to *DE*.

In comparison with the calculated eigenfrequencies and taking into account all different wavelengths, we can identify all of the 13 expected E_2 modes in both configurations and confirm all expected Raman modes for the paramagnetic state. We note that the scattering intensity of the modes depends on the used laser wavelength. This constitutes again the first class of identified modes. The second class contains one mode, which emerges upon cooling below T_N and can be identified as mode $E_1(3)$ in agreement with the selection rules and corepresentations of the magnetic point group $6'm'm$. For the third class of modes, we have to distinguish between the Raman configurations $z(xx)\bar{z}$ and $z(yx)\bar{z}$. In the $z(xx)\bar{z}$ configuration the A_1 modes are allowed at both temperatures and the three $A_1(i)$ modes with i = 1, 3, 7 can be identified in comparison with the observed TO eigenfrequencies for $\mathbf{E}^{\omega}||c$ and $y(zz)\bar{y}$ in Fig. 2 and Table 2 at all used laser frequencies. In contrast, the fact that these three modes appear also in the $z(yx)\bar{z}$ configuration, both at 295 K and below T_N for a wavelength of 532 nm and in a less systematic way for the other wavelengths, indicates again a breaking of selection rules

Table 3 | Raman excitations for $z(yx)\bar{z}$ and $z(xx)\bar{z}$

Raman $z(xy)\bar{z}$								Mode	Raman $z(xx)\bar{z}$							
632.8 nm		532 nm		514.3 nm		473 nm		assignment	632.8 nm		532 nm		514.3 nm		473 nm	
300 K	5 K	295 K	10 K	300 K	5 K	300 K	5 K	$E_2(i)$ i = 1, …, 13 (calc.)	300 K	5 K	295 K	10 K	300 K	5 K	300 K	5 K
70	*71*	*71*	*71*	*71*	*73*	*70*	*71*	71	*70*	*71*	*71*	*71*	*71*	*72*	*70*	*71*
150	*151*	–	–	–	–	–	–	148	*149*	*151*	–	–	–	–	–	–
193	–	*195*	*196*	*194*	*197*	–	–	191	*193*	*195*	*195*	*196*	*194*	*196*	–	–
215	*217*	*217*	*219*	*217*	*219*	*216*	*217*	215	*216*	*217*	*217*	*219*	*216*	*219*	*216*	*217*
276	*276*	*278*	*278*	*278*	*279*	*277*	*275*	263	*277*	*276*	*278*	*278*	*277*	*278*	*276*	*277*
337	*335*	*335*	*337*	*335*	*337*	*337*	*336*	332	*333*	*334*	*335*	*337*	*337*	*337*	*335*	*335*
348	*346*	*348*	*347*	*347*	*349*	*349*	*347*	357	*348*	*347*	*348*	*347*	*349*	*349*	*347*	*348*
–	–	*449*	*450*	*449*	*451*	–	*450*	458	*449*	*449*	*449*	*450*	*449*	*452*	*450*	*450*
–	–	–	–	*476*	*476*	–	–	472	*476*	*475*	–	–	–	–	–	–
482	*483*	*484*	*485*	*484*	*485*	*483*	*483*	482	*483*	*483*	*484*	*485*	*484*	*486*	*484*	*482*
519	–	*522*	*522*	*521*	*522*	*520*	*522*	531	–	*520*	*522*	*522*	–	*523*	*521*	*521*
565	*566*	*564*	*565*	*566*	*567*	*565*	*566*	570	*566*	*566*	*564*	*565*	*565*	*568*	*566*	*566*
739	*739*	*738*	*739*	*738*	*740*	*738*	*739*	764	*737*	*737*	*738*	*739*	*737*	*741*	*737*	*738*
–	*227*	–	*229*	–	*228*	–	–	$E_1(3)$ at 229 (exp.)	–	*226*	–	*229*	–	–	–	*227*
–	208	205	208	–	–	–	–	$A_1(1)$ at 207 (TO)	*205*	*207*	*205*	*208*	*206*	*208*	*206*	*207*
–	–	373	374	372	376	–	375	$A_1(3)$ at 372 (TO)	*373*	*373*	*373*	*374*	*373*	*376*	*374*	*374*
–	656	654	656	–	653	–	655	$A_1(7)$ at 655 (TO)	*655*	*657*	*654*	*656*	*654*	*660*	*655*	*657*
–	212	–	–	–	–	–	–	$A_1(1)$ (LO*)	–	–	–	–	–	–	–	–
–	–	–	–	–	–	–	–	$A_1(2)$ at 286 (LO)	285	–	–	–	–	–	–	284
–	–	–	505	–	506	–	–	$A_1(5)$ at 505 (LO)	–	503	505	505	–	506	502	504
–	–	–	–	–	–	–	–	$A_1(6)$ at 582 (LO)	578	580	578	582	578	582	579	580
–	–	–	820	–	–	–	–	$A_1(9)$ at 824 (LO)	820	821	820	820	818	823	819	820
–	–	–	303	–	–	–	–	electronic	–	300	–	303	–	305	–	304
–	361	–	361	–	362	–	361	electronic	–	360	–	361	–	363	–	–
–	–	291	–	–	–	–	–	not identified	293	–	291	–	–	–	290	–

Experimental Raman excitation frequencies in $Co_2Mo_3O_8$ (in cm^{-1}) measured in $z(yx)\bar{z}$ and $z(xx)\bar{z}$ configuration in the paramagnetic phase (at 295 K or 300 K) and at low temperatures in the magnetically ordered phase (at 5 K or 10 K) with different laser frequencies. Mode assignment is made by comparison with calculated phonon eigenfrequencies obtained from ab initio calculations for the 13 expected E_2 modes and by comparing to experimental values from other measurements configurations. Numbers in italic fonts indicate the allowed observed modes.

already at room temperature in the same way as the A_1 modes observed in the forbidden Raman configuration $y(xz)\bar{y}$. As before, we assign their occurrence to resonant Raman scattering effects unrelated to magnetic ordering, which is again accompanied by the appearance of LO A_1 modes in both Raman configurations. In particular, we observe four modes at the LO frequencies of the $A_1(i)$ modes with i = 2, 5, 6, 9, with mode $A_1(9)$ (LO) having appeared also for $y(xz)\bar{y}$. Along this line, we tentatively assign the single appearance of the mode at 212 cm^{-1} at 300 K with a laser wavelength of 632.8 nm to the LO eigenfrequency of $A_1(1)$. This mode was not observed in the IR reflectivity spectrum and, hence, its LO frequency is unknown, but the observed mode is slightly higher than the TO eigenfrequency of $A_1(1)$ at about 206 cm^{-1}, making this assignment a reasonable choice. The fourth class consists of the two electronic excitations below T_N at 303 cm^{-1} and 363 cm^{-1} already discussed above. Finally, we are left with only one unidentifed excitation at 291 cm^{-1}, which is clearly visible only at some laser wavelengths and close to room temperature. Notably, this mode can be compared to the $E_1(4)$ mode identified at 291 cm^{-1} in the $y(xz)\bar{y}$ configuration and the corresponding IR reflectivity data (Table 2). The temperature dependences of the Raman spectra taken at 532 nm in $z(xx)\bar{z}$ and $y(xz)\bar{y}$ configurations are compared in Fig. 3. While in $y(xz)\bar{y}$ configuration the $E_1(4)$ mode is visible at all temperatures and does not shift strongly with temperature (Fig. 3b), the mode at 291 cm^{-1} in $z(xx)\bar{z}$ is clearly much broader at 300 K than the allowed $E_1(4)$ mode and additionally broadens with decreasing temperature and evolves into an enhanced background plateau, while the electronic mode at 304 cm^{-1} emerges. At present, the origin of this behavior remains unclear and may be investigated in the future.

Finally, we want to emphasize that all 34 expected A_1, E_1, and E_2 modes of the paramagnetic phase could be identified in corresponding Raman and IR configurations. Moreover, the observation of $E_2(1)$, $E_2(5)$ and $E_2(6)$ in $y(xz)\bar{y}$ and the observation of $E_1(3)$ in $z(xy)\bar{z}$ and in $z(xx)\bar{z}$ only in the magnetically ordered state can be counted as a fivefold confirmation of the predicted selection rules of irreducible corepresentations by Raman scattering. In addition, mode $E_2(1)$ has also been observed independently by THz-transmission spectroscopy, adding up to a sixfold confirmation of the magnetic point group selection rules. The overall number of 39 correctly assigned modes in $Co_2Mo_3O_8$ below T_N is, in our opinion, remarkable.

Discussion

We studied the optical phonons of $Co_2Mo_3O_8$ in its paramagnetic and collinear antiferromagnetic phases by IR- and Raman spectroscopy. We find that (i) we can detect all expected optical phonon modes of the paramagnetic phase in either the IR- or the Raman and, in most cases, both channels, (ii) their eigenfrequencies are in excellent agreement with values obtained by ab initio calculations, and most importantly, (iii) the changes of the IR and Raman selection rules induced by the emergence of the antiferromagnetic

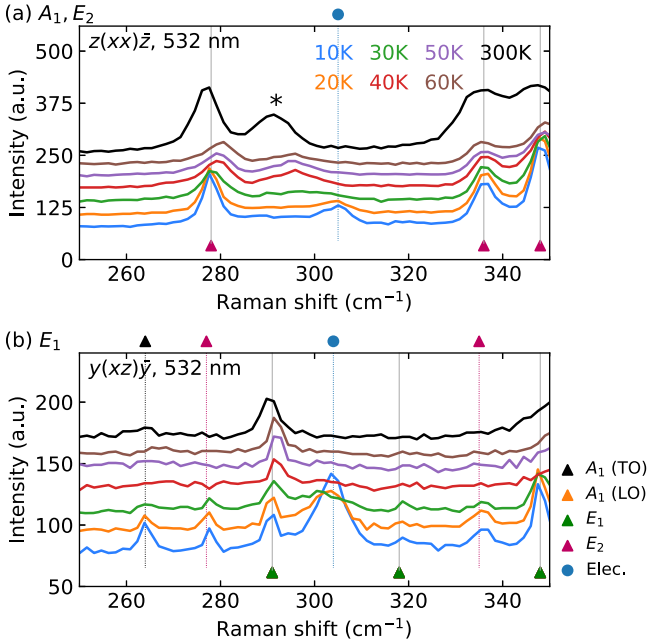

Fig. 3 | Temperature dependent Raman spectra. Temperature dependence of the Raman spectra in **a** $z(xx)\bar{z}$ configuration and **b** $y(xz)\bar{y}$ configuration in the vicinity of the $E_1(4)$ mode at around 290 cm^{-1} and the electronic mode at around 304 cm^{-1}. The mode assignment follows the same colorscheme as in Fig. 2.

state follow the predictions derived from irreducible corepresentations of the relativistic magnetic point group.

In particular, the last two points show that relativistic effects are necessary to capture the essential physics of optical phonons in $Co_2Mo_3O_8$. This contrasts with the phonon selection rules derived for a spin-orbit-free altermagnetic ground state in $Co_2Mo_3O_8$, where non-relativistic spin-group symmetries predict that the phonon selection rules remain unchanged across the magnetic phase transition. A reanalysis of the IR- and Raman eigenfrequencies published in Refs. 37,40 for the sister compound $Fe_2Mo_3O_8$ is discussed in Supplement section II and listed in Tables SVII–SIX. This comparison confirms this result with three E_2 modes and one E_1 mode appearing below T_N as a result of magnetic symmetry breaking. In addition, both compounds reportedly show non-reciprocal directional dichroism[25,32], which is an optical magnetoelectric effect that is not allowed in the spin group approach. This is consistent with its interpretation as a relativistic correction to the Cotton–Mouton effect[50].

Finally, we highlight that our approach to study optical phonons - used to test the symmetries of phonon excitations and phonon-magnon interactions in magnetically ordered materials - is not limited to insulating collinear altermagnets. It applies to all magnetic compounds described within the spin-group framework. However, this method provides only a necessary, not a sufficient, condition for determining whether magnon excitations obey non-relativistic symmetries. This also raises the interesting question of the extent to which optical phonons can be used to test the symmetries of electronic excitations, which we leave for future investigation.

Methods

Reflectivity and transmission measurements

Reflectivity measurements were performed on an as-grown *ab*-plane single crystal and on an *ac*-cut mosaic sample composed of two single crystals. Transmission measurements were performed on a thin *ab*-plane single crystal. By using a Bruker Fourier-transform IR-spectrometer Vertex80 equipped with a He-flow cryostat, the frequency range from 100 to 13,000 cm^{-1} and a temperature range from 5 to 300 K could be covered. Terahertz (THz) time-domain spectroscopy measurements were performed using a TOPTICA TeraFlash system as described in Ref. 25.

Raman scattering

Raman scattering spectra were recorded in backscattering geometry using a Jobin Yvon LabRam HR800 micro-spectrometer. A 532 nm laser with a power of 370 µW on the sample was employed as the excitation source with an acquisition time of 120 × 3 s. Focusing was performed using a 50× microscope objective. The samples were placed in a cryostat, which enabled measurements over a wide temperature range. Measurements in $z(yx)\bar{z}$ and $z(xx)\bar{z}$ configurations were performed on an *ab*-plane cut single crystal and measurement in $y(xz)\bar{y}$ and $y(zz)\bar{y}$ configurations were performed on an *ac*-plane cut single crystal.

All Raman spectra with 632.8, 514.3, 473 nm wavelengths were recorded using a Trivista 777 spectrometer in single-stage configuration, equipped with a Nitrogen-cooled, ultra-low-noise PyLoN CCD detector. A diffraction grating with 1800 grooves/mm was used, yielding a spectral resolution better than 0.3 cm^{-1}. Typical acquisition time was 600 s for all the measurements. The measurements were carried out using three different excitation sources: a He-Ne laser with wavelength $\lambda = 632.8$ nm (1.95 eV), and two diode-pumped solid-state lasers with $\lambda = 514.3$ nm (2.41 eV) and $\lambda = 473$ nm (2.62 eV). The excitation beam was focused onto the sample using a 50× long-working-distance objective lens with a numerical aperture (NA) of 0.55, with an approximate spot size of 2 µm. To suppress the Rayleigh scattering and achieve a low-energy cutoff, three volume Bragg filters were employed, each optimised for the respective excitation wavelength. The laser power incident on the sample was maintained at ~300 µW for all measurements. Low-temperature measurements were conducted using a Janis liquid helium (LHe)-based cold-finger cryostat operating under a vacuum of 5×10^{-5} mbar.

DFT calculations

Density-functional-theory (DFT) band-structure calculations were performed in the Vienna Ab initio Simulation Package code[51,52] using the Perdew-Burke-Ernzerhof version of the exchange-correlation potential[53]. Phonon frequencies at the Γ-point were obtained by the finite-displacement method. Electronic correlations in the Co 3*d* shell were taken into account on the mean-field level using the DFT+U procedure with the on-site Coulomb repulsion parameter U_d = 5 eV and Hund's coupling J_d = 1 eV[28]. The experimental collinear antiferromagnetic configuration was used, and spin-orbit (SO) coupling was included in order to reproduce the large magnetic anisotropy on the octahedrally coordinated Co^{2+} site.

Data availability

The IR, Raman, and THz spectra are available on Zenodo https://doi.org/10.5281/zenodo.17663262.

Received: 7 August 2025; Accepted: 25 January 2026;
Published online: 17 February 2026

References

1. Šmejkal, L., Sinova, J. & Jungwirth, T. Beyond conventional ferromagnetism and antiferromagnetism: a phase with nonrelativistic spin and crystal rotation symmetry. *Phys. Rev. X* **12**, 031042 (2022).
2. Bhowal, S. & Spaldin, N. A. Ferroically ordered magnetic octupoles in d-wave altermagnets. *Phys. Rev. X* **14**, 011019 (2024).
3. Morano, V. C. et al. Absence of altermagnetic magnon band splitting in MnF_2. *Phys. Rev. Lett.* **134**, 226702 (2025).
4. Yu, B.-W. & Liu, B.-G. Spin-split flat bands at the band edge and two-dimensional hole gases towards quantum Hall effect in altermagnetic CoF_2. Preprint at https://arxiv.org/abs/2411.16188 (2024).
5. Dubrovin, R. M. et al. Polar phonons and magnetic excitations in the antiferromagnet CoF_2. *Phys. Rev. B* **109**, 224312 (2024).
6. Lee, S. et al. Broken Kramers degeneracy in altermagnetic MnTe. *Phys. Rev. Lett.* **132**, 036702 (2024).
7. Krempaský, J. et al. Altermagnetic lifting of Kramers spin degeneracy. *Nature* **626**, 517 (2024).

8. Liu, Z., Ozeki, M., Asai, S., Itoh, S. & Masuda, T. Chiral split magnon in altermagnetic MnTe. *Phys. Rev. Lett.* **133**, 156702 (2024).
9. Jost, D. et al. Chiral altermagnon in MnTe. Preprint at https://arxiv.org/abs/2501.17380 (2025).
10. Fedchenko, O. et al. Observation of time-reversal symmetry breaking in the band structure of altermagnetic RuO_2. *Sci. Adv.* **10**, adj4883 (2024).
11. Wenzel, M. et al. Fermi-liquid behavior of nonaltermagnetic RuO_2. *Phys. Rev. B* **111**, l041115 (2025).
12. Liu, J. et al. Absence of altermagnetic spin splitting character in rutile oxide RuO_2. *Phys. Rev. Lett.* **133**, 176401 (2024).
13. Naish, V. E. On magnetic symmetry of crystals. *Izv. Akad. Nauk SSSR* **27**, 1496 (1963).
14. Brinkman, W. F. & Elliott, R. J. Theory of spin-space groups. *Proc. R. Soc. Lond. Ser. A Math. Phys. Sci.* **294**, 343 (1966).
15. Litvin, D. & Opechowski, W. Spin groups. *Physica* **76**, 538 (1974).
16. Litvin, D. B. Spin point groups. *Acta Crystallogr. Sect. A* **33**, 279 (1977).
17. Bradley, C. J. & Cracknell, A. P. *The Mathematical Theory Of Symmetry In Solids: Representation theory for point groups and space groups* (Oxford University PressOxford, 2009). https://doi.org/10.1093/oso/9780199582587.001.0001.
18. Kurumaji, T., Ishiwata, S. & Tokura, Y. Doping-tunable ferrimagnetic phase with large linear magnetoelectric effect in a polar magnet $Fe_2Mo_3O_8$. *Phys. Rev. X* **5**, 031034 (2015).
19. Wang, Y. et al. Unveiling hidden ferrimagnetism and giant magnetoelectricity in polar magnet $Fe_2Mo_3O_8$. *Sci. Rep.* **5**, 12268 (2015).
20. Kurumaji, T., Ishiwata, S. & Tokura, Y. Diagonal magnetoelectric susceptibility and effect of Fe doping in the polar ferrimagnet $Mn_2Mo_3O_8$. *Phys. Rev. B* **95**, 045142 (2017).
21. Tang, Y. S. et al. Collinear magnetic structure and multiferroicity in the polar magnet $Co_2Mo_3O_8$. *Phys. Rev. B* **100**, 134112 (2019).
22. Csizi, B. et al. Magnetic and vibronic terahertz excitations in Zn-doped $Fe_2Mo_3O_8$. *Phys. Rev. B* **102**, 174407 (2020).
23. Tang, Y. S. et al. Metamagnetic transitions and magnetoelectricity in the spin-1 honeycomb antiferromagnet $Ni_2Mo_3O_8$. *Phys. Rev. B* **103**, 014112 (2021).
24. Tang, Y. S. et al. Successive electric polarization transitions induced by high magnetic field in the single-crystal antiferromagnet $Co_2Mo_3O_8$. *Phys. Rev. B* **105**, 064108 (2022).
25. Reschke, S. et al. Confirming the trilinear form of the optical magnetoelectric effect in the polar honeycomb antiferromagnet $Co_2Mo_3O_8$. *npj Quantum Mater.* **7**, 1 (2022).
26. Prodan, L. et al. Dilution of a polar magnet: structure and magnetism of Zn-substituted $Co_2Mo_3O_8$. *Phys. Rev. B* **106**, 174421 (2022).
27. Ghara, S. et al. Magnetization reversal through an antiferromagnetic state. *Nat. Commun.* **14**, 5174 (2023).
28. Szaller, D. et al. Coexistence of antiferromagnetism and ferrimagnetism in adjacent honeycomb layers. *Phys. Rev. B* **111**, 184404 (2025).
29. Kurumaji, T. et al. Electromagnon resonance in a collinear spin state of the polar antiferromagnet $Fe_2Mo_3O_8$. *Phys. Rev. B* **95**, 020405(R) (2017).
30. Wu, F. et al. Fluctuation-enhanced phonon magnetic moments in a polar antiferromagnet. *Nat. Phys.* **1868** https://doi.org/10.1038/s41567-023-02210-4 (2023).
31. Bao, S. et al. Direct observation of topological magnon polarons in a multiferroic material. *Nat. Commun.* **14**, 6093 (2023).
32. Vasin, K. V. et al. Optical magnetoelectric effect in the polar honeycomb antiferromagnet $Fe_2Mo_3O_8$. *Phys. Rev. B* **110**, 054401 (2024).
33. Cheong, S.-W. & Huang, F.-T. Altermagnetism with non-collinear spins. *npj Quantum Mater.* **9**, 13 (2024).
34. Chen, X. et al. Unconventional magnons in collinear magnets dictated by spin space groups. *Nature* **640**, 349 (2025).
35. Varret, F., Czeskleba, H., Hartmann-Boutron, F. & Imbert, P. Étude par effet Mössbauer de lion Fe^{2+} en symétrie trigonale dans les composés du type $(Fe, M)_2Mo_3O_8$ (M = Mg, Zn, Mn, Co, Ni) et propriétés magnétiques de $(Fe, Zn)_2Mo_3O_8$. *J. Phys.* **33**, 549 (1972).
36. Cotton, F. A. Metal atom clusters in oxide systems. *Inorg. Chem.* **3**, 1217 (1964).
37. Reschke, S. et al. Structure, phonons, and orbital degrees of freedom in $Fe_2Mo_3O_8$. *Phys. Rev. B* **102**, 094307 (2020).
38. McClarty, P. A. & Rau, J. G. Landau theory of altermagnetism. *Phys. Rev. Lett.* **132**, 176702 (2024).
39. Schiff, H., McClarty, P., Rau, J. G. & Romhányi, J. Collinear altermagnets and their Landau theories. *Phys. Rev. Res.* **7**, 033301 (2025).
40. Stanislavchuk, T. N. et al. Spectroscopic and first principle DFT +eDMFT study of complex structural, electronic, and vibrational properties of $M_2Mo_3O_8$ (M = Fe, Mn) polar magnets. *Phys. Rev. B* **102**, 115139 (2020).
41. Cracknell, A. P. Scattering matrices for the Raman effect in magnetic crystals. *J. Phys. C Solid State Phys.* **2**, 500 (1969).
42. Schiff, H., Corticelli, A., Guerreiro, A., Romhányi, J. & McClarty, P. A. The crystallographic spin point groups and their representations. *SciPost Phys.* **18**, 109 (2025).
43. Jaeschke-Ubiergo, R., Bharadwaj, V. K., Jungwirth, T., Šmejkal, L. & Sinova, J. Supercell altermagnets. *Phys. Rev. B* **109**, 094425 (2024).
44. Hayes, W. & Loudon, R. *Scattering of Light by Crystals* (Dover, 2004).
45. Manuel Cardona, G. G. ed. *Light Scattering in Solids II* (Springer Berlin Heidelberg, 1982) https://doi.org/10.1007/3-540-11380-0.
46. Shapiro, S. M. & Axe, J. D. Raman Scattering from Polar Phonons. *Phys. Rev. B* **6**, 2420 (1972).
47. Ovander, L. N. & Tyu, N. S. Theory of Raman scattering on polar phonons. *Phys. Status Solidi B* **91**, 763 (1979).
48. Martin, R. M. & Damen, T. C. Breakdown of selection rules in resonance Raman scattering. *Phys. Rev. Lett.* **26**, 86 (1971).
49. Trallero-Giner, C., Cantarero, A. & Cardona, M. One-phonon resonant Raman scattering: Fröhlich exciton-phonon interaction. *Phys. Rev. B* **40**, 4030 (1989).
50. Rikken, G. L. J. A., Strohm, C. & Wyder, P. Observation of magnetoelectric directional anisotropy. *Phys. Rev. Lett.* **89**, 133005 (2002).
51. Kresse, G. & Furthmüller, J. Efficiency of ab-initio total energy calculations for metals and semiconductors using a plane-wave basis set. *Comput. Mater. Sci.* **6**, 15 (1996).
52. Kresse, G. & Furthmüller, J. Efficient iterative schemes for ab initio total-energy calculations using a plane-wave basis set. *Phys. Rev. B* **54**, 11169 (1996).
53. Perdew, J. P., Burke, K. & Ernzerhof, M. Generalized gradient approximation made simple. *Phys. Rev. Lett.* **77**, 3865 (1996).

Acknowledgements

M.K. and K.P. thank Hana Schiff for stimulating discussions. This research was partly funded by the Deutsche Forschungsgemeinschaft (DFG, German Research Foundation)-TRR 360-492547816. The support by 0.25 N within the project ANCD (cod 011201 Moldova) is also acknowledged. The authors gratefully acknowledge the use of computing resources of the ALCC HPC cluster (Institute of Physics, University of Augsburg). We acknowledge the support of the LNCMI-CNRS, member of the European Magnetic Field Laboratory (EMFL). This research was supported by the Ministry of Culture and Innovation and the National Research, Development and Innovation Office within the Quantum Information National Laboratory of Hungary (Grant No. 2022-2.1.1-NL-2022-00004) as well as the Hungarian NKFIH Grant No. K 142652 and FK135003. M.K. was partially funded by the scholarship program DKÖP-25-1-BME-25 of NKFIH and Budapest University of Technology and Economics.

Author contributions

L.P. and V.T. synthesized and characterized the crystals; F.S., O.E., and K.V. measured the reflectivity and transmission spectra; D.U., A.P., C.F. and P.L. measured the Raman spectra; F.S., K.V., O.E. and J.D. analyzed the data; A.A.T. performed the ab initio calculations; M.K., K.P., S.B. and J.D. performed the group theoretical analysis; F.S., M.K., K.P., S.B. and J.D. wrote the paper; I.K., S.B. and J.D. planned and coordinated the project; All authors contributed to the discussion and interpretation of the experimental and theoretical results and to the completion of the paper.

Funding

Open Access funding enabled and organized by Projekt DEAL.

Competing interests

The authors declare no competing interests.

Additional information

Supplementary information The online version contains supplementary material available at https://doi.org/10.1038/s41535-026-00857-9.

Correspondence and requests for materials should be addressed to F. Schilberth or J. Deisenhofer.